Journal of Energy Storage 96 (2024) 112628

Contents lists available at ScienceDirect

Journal of Energy Storage

journal homepage: www.elsevier.com/locate/est

Research papers

Sliding mode observer with adaptive switching gain for estimating state of charge and internal temperature of a commercial Li-ion pouch cell

Behnam Ghalami Choobar [a], Hamid Hamed [a,b], Mohammadhosein Safari [a,b,c,*]

[a] Institute for Materials Research (IMO-imomec), UHasselt, Martelarenlaan 42, B-3500 Hasselt, Belgium
[b] Energyville, Thor Park 8320, B-3600 Genk, Belgium
[c] IMEC division IMOMEC, BE-3590, Belgium

ARTICLE INFO

Keywords:
Lithium-ion batteries
State of charge
Sliding mode observer
Coupled equivalent circuit model

ABSTRACT

Accurate estimation of the state of charge (SOC) and internal temperature is the essence of the battery management systems for lithium-ion batteries (LIBs). In this research, an improved sliding mode observer (SMO) is presented and evaluated for the estimation of SOC and internal temperature of LIBs by adapting the switching gain. The observer is meticulously designed, parametrized, and validated by combining modeling and experimentation on a commercial 64 Ah LIB pouch cell. The battery behavior is emulated by a coupled equivalent circuit model (CECM) composed of a dual-polarization and a novel thermal model. The proposed observer is showcased to estimate the SOC with an average error of <2 % even in the presence of a significant model mismatch. The results provide deep insight into the development process of the efficient and robust SMO observers for estimating the internal states of LIBs.

1. Introduction

Modeling of the battery behavior is necessary to develop, understand, design, and optimize the existing and new battery technologies. Mathematical models allow a thorough analysis of the almost unlimited design parameters and operational conditions at a relatively small cost. Numerous modeling strategies have been proposed in the literature [1–4]. These models might be classified as (1) physics-independent, (2) semi-physics-based, and (3) physics-based models [1]. Semi-physics-based models, known as gray boxes, provide an alternative representation of the physical entity. The most famous alternative battery models are equivalent circuit models (ECM) [5], in which electrical elements represent the physical processes inside a battery cell. Among equivalent circuit models, the dual polarization model, due to well-adjusted accuracy and computational complexity [6], is frequently used as a design model in the online observers to estimate the internal variables of lithium-ion batteries (LIBs) such as state of charge (SOC) [7]. There is a wide range of thermal models proposed for LIBs among which the physics-based [8], data-driven [9,10], and thermal resistance models [11] are noteworthy from the recent literature. Particularly, the latter type of models is a feasible candidate for on-line prediction purposes owing to its simple structure and minimal computational demands [12].

The SOC of a LIB might be defined as the ratio of the remaining charge inside the anode to the nominal capacity of the cell. Various model-based [7] and data-driven [13] estimation methods have been established to estimate the SOC since its direct experimental measurement is not straightforward. Model-based methods treat the SOC as a state variable and employ a variety of algorithms to estimate the SOC such as the Kalman filter (KF), extended Kalman filter (EKF) [14,15], unscented Kalman filter (UKF) [15–17], H-infinity filter [18,19], proportional integral observer (PIO) [20], sliding mode observer (SMO) [6,21] and other nonlinear observers. On the other hand, the data-driven methods use statistical or machine learning techniques to estimate the SOC from the relatively massive historical or real-time data, such as artificial neural networks (ANN) [22], support vector machines (SVM) [23], fuzzy logic [24,25], and adaptive neuro-fuzzy inference system (ANFIS) [26].

The performance and reliability of the SOC estimation algorithms based on KF rely on the accuracy of both the underlying models and the measurements, which are often uncertain and noisy, respectively [27,28]. These algorithms are developed based on two assumptions. First, that the battery model is accurate, and second, that the noise distribution is known. These assumptions make these algorithms less resilient and more computationally demanding for online applications.

* Corresponding author at: Institute for Materials Research (IMO-imomec), UHasselt, Martelarenlaan 42, B-3500 Hasselt, Belgium.
E-mail address: momo.safari@uhasselt.be (M. Safari).

https://doi.org/10.1016/j.est.2024.112628
Received 15 March 2024; Received in revised form 31 May 2024; Accepted 16 June 2024
Available online 24 June 2024
2352-152X/© 2024 Elsevier Ltd. All rights are reserved, including those for text and data mining, AI training, and similar technologies.

SMO, on the other hand, is a robust and efficient algorithm that can ensure the stability and robustness of the system against model uncertainties and external disturbances based on the Lyapunov function analysis [29]. Additionally, its simplicity and ease of implementation are very attractive aspects for online applications. For instance, Xu et al. developed an adaptive sliding mode observer for SOC estimation of a liquid metal battery [30]. They applied a recursive least square algorithm to identify the ECM model's parameters. They showed that their observer with a new adaptation law had faster convergence, higher accuracy, stronger robustness, and lower computational cost than other methods. To cite another example, Fereydooni et al. [6] proposed a novel adaptive sliding mode with a geometrical control-based adaptation law for the internal resistance. They used a P2D model to evaluate the performance of the observer and demonstrated a higher accuracy and lower computational cost for the SMO relative to the EKF in estimating the SOC of a cylindrical battery. Notwithstanding the rich literature of the state estimation for lithium-ion batteries, prior investigations often solely adopt the ECM as the design model, overlooking the thermal effects on the model parameters [30–35]. Some investigations employ an uncoupled structure for estimating the SOC and internal temperature which is computationally limited in capturing the intricate interactions between the charge and thermal states of the cell [11,36–39]. Moreover, the experimental validation of the proposed models is frequently disregarded in the available literature which complicates the assessment of the predictions against model uncertainties and measurement noise [6,21,30,33].

Here, a novel approach is introduced to estimate the SOC and temperature of a 64 Ah commercial lithium-ion pouch cell (Fig. 1a) using an adaptive gain SMO (Fig. 1c). The characteristics of the examined cell are outlined in Appendix B. The observer design is based on a coupled equivalent circuit model (CECM) that combines a dual polarization ECM (Fig. 1b) and a simple thermal model. The observer is parametrized and validated using the experimental voltage and surface temperature profiles of the Li-ion pouch cell collected at three different temperatures and state-of-health (Fig. 1d).

2. Battery modeling

The dual polarization ECM model is used to simulate the electrochemical behavior of the lithium-ion pouch cell. An ECM typically comprises three major parts: a static part to represent the OCV as a function of SOC and temperature; a dynamic part represented with a combination of RC elements to emulate the kinetics and charge transport limitations of the cell; and a source or load to simulate the closed circuit for charge and discharge regimes. In the subsequent section, the equations of the coupled equivalent circuit model (CECM) are detailed.

2.1. Battery coupled equivalent circuit model (CECM)

The configuration of the dual polarization model is presented in Fig. 1b. R_s^e represents the internal ohmic resistance of the cell. The two RC branches, including two pure resistance elements, R_1^e and R_2^e, and two ideal capacitor elements, C_1^e and C_2^e, account for the kinetics and transport limitations inside the cell. E_0 represents the equilibrium voltage (OCV) of the cell. All the model parameters depend on the SOC and operational conditions and considered to be functions of both the SOC and the average of surface and core temperatures of the battery ($T = \frac{T_c+T_s}{2}$).

According to Kirchhoff's voltage law in circuit theory, the cell voltage, V_0, can be written as

$$V_0 = E_0 - V_1(t) - V_2(t) - I(t)R_s^e \quad (1)$$

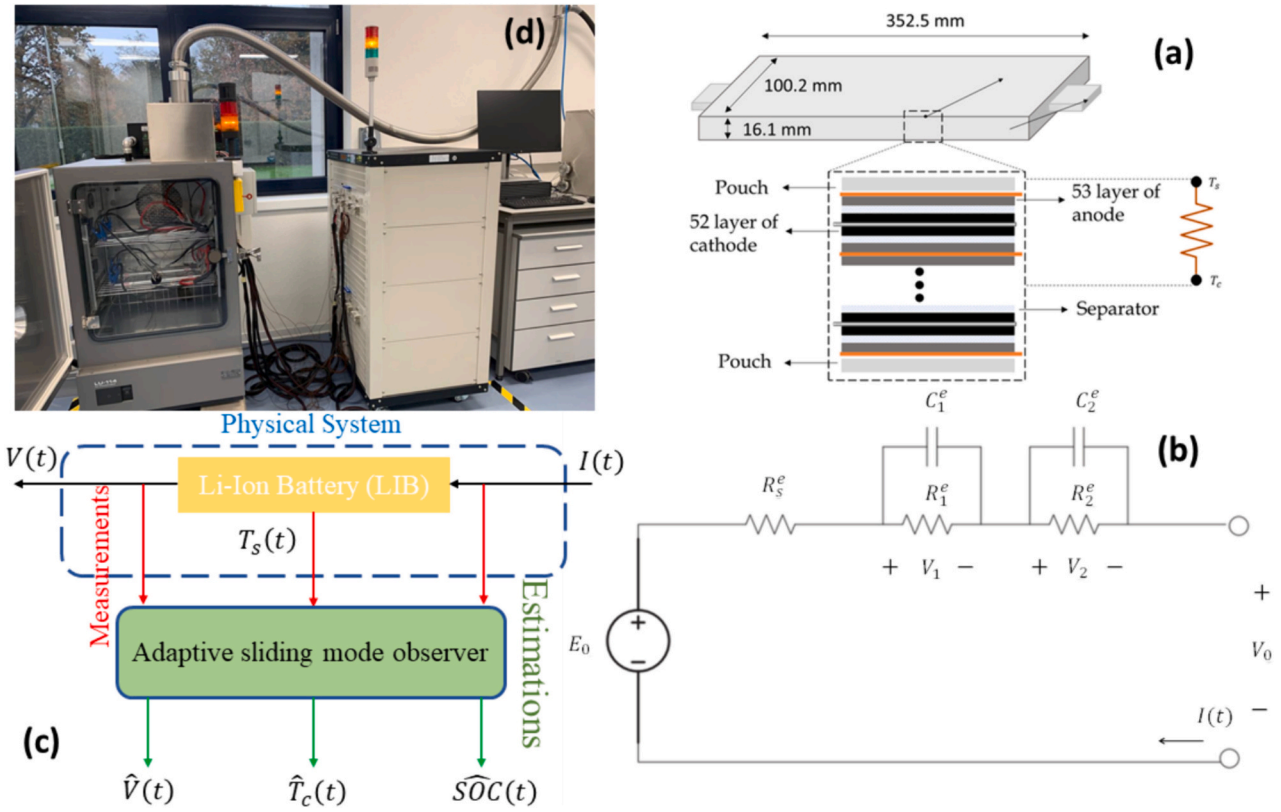

Fig. 1. The experimentation and modeling methodology for the development of the SMO observer to predict the SOC and core temperature of the **(a)** 64 Ah Gr/NMC commercial Li-ion pouch cell, **(b)** dual-polarization ECM model, **(c)** SMO structure, **(d)** the experimental platform and instrumentation: battery cycler, explosion-proof thermal chamber.

where V_1 and V_2 are the voltage drops across the first and second RC branches, respectively, of which the time derivatives read

$$\dot{V}_1 = -\frac{V_1(t)}{R_1^e C_1^e} + \frac{I(t)}{C_1^e} \tag{2}$$

$$\dot{V}_2 = -\frac{V_2(t)}{R_2^e C_2^e} + \frac{I(t)}{C_2^e} \tag{3}$$

Assuming Z_0 to be the initial SOC of the battery at t_0, the instantaneous SOC of the battery (Z) with a nominal capacity of C_n^e at a given time t is

$$Z(t) = Z_0 + \int_{t_0}^{t} \frac{I(\tau)}{C_n^e} d\tau \tag{4}$$

Following Eq. (4), the derivative of the SOC with respect to time ($\dot{Z}$) can be expressed as

$$\dot{Z} = -\frac{I(t)}{C_n^e} \tag{5}$$

The other state variables, the surface and core temperatures, are linked to the electrical model parameters through a lumped simplified thermal model. In this model, the thermal behavior of the battery is approximated by two nodes at the surface (T_s) and center of the cell (T_c). The dynamics of temperature at these two nodes can be described by considering the irreversible and reversible sources of heat generation [40] and heat exchange between the two nodes as well as that between the surface node and the cell exterior

$$\dot{T}_c = \frac{I(E_0 - V_0)}{2C_c^t} - \frac{I(T_c + T_s)\Delta S}{2FC_c^t} + \frac{T_s - T_c}{R_c^t C_c^t} \tag{6}$$

$$\dot{T}_s = \frac{I(E_0 - V_0)}{2C_s^t} - \frac{I(T_c + T_s)\Delta S}{2FC_s^t} + \frac{T_c - T_s}{R_c^t C_s^t} + \frac{(T_f - T_s)}{R_f^t C_s^t} \tag{7}$$

where T_f is the ambient temperature, R_f^t is the convection thermal resistance between the cell and exterior, F is Faraday's constant (96,485 C/mol), R_c^t is the conduction thermal resistance inside the battery, and the C_c^t and C_s^t are the heat capacity of the internal and surface nodes, respectively. Also, ΔS represents overall entropy change of the anodic and cathodic reactions and can be expressed by $\Delta S = F\frac{\partial E_0}{\partial T}$. As will be discussed later, a key assumption for the observability of the design model is that both of core and surface nodes contribute to the heat generation of the cell.

The electrochemical and thermal models should be solved simultaneously to enable an accurate prediction of the SOC. To develop an observable form of our model equations, we need to derive an explicit form of the derivative of the model variables. To simplify the calculations, it is assumed that E_0 has a piecewise linear dependency on Z and T: $E_0 = \kappa_1 T + \kappa_2 Z + \kappa_3$, where T is the average of surface and core temperatures. Therefore, entropy change (ΔS) in Eqs. (6) and (7) can be substituted by $F\kappa_1$. Consquently, the observable equation set of the CECM can be represented by combining Eq. (1) with Eqs. (2)–(5):

$$\begin{aligned}
\dot{V}_0 = {} & -\frac{\kappa_2}{R_s^e C_n^e} V_0 + \left(\frac{1}{R_1^e C_1^e} - \frac{\kappa_2}{R_s^e C_n^e}\right) V_1 + \left(\frac{1}{R_2^e C_2^e} - \frac{\kappa_2}{R_s^e C_n^e}\right) V_2 + \frac{{\kappa_2}^2}{R_s^e C_n^e} Z \\
& + \left(\frac{\kappa_1 \kappa_2}{2R_s^e C_n^e} - \frac{\kappa_1}{2R_c^t}\left(\frac{1}{C_c^t} - \frac{1}{C_s^t}\right)\right) T_c + \left(\frac{\kappa_1 \kappa_2}{2R_s^e C_n^e}\right. \\
& \left. - \frac{\kappa_1}{2}\left(\frac{1}{R_c^t C_c^t} - \frac{1}{R_c^t C_s^t} + \frac{1}{R_f^t C_s^t}\right)\right) T_s + \left(-\frac{\kappa_1}{4}\left(\frac{1}{C_c^t} + \frac{1}{C_s^t}\right) V_0\right. \\
& + \frac{\kappa_1 \kappa_2}{4}\left(\frac{1}{C_c^t} + \frac{1}{C_s^t}\right) Z - \frac{{\kappa_1}^2}{8}\left(\frac{1}{C_c^t} + \frac{1}{C_s^t}\right) T_c - \frac{{\kappa_1}^2}{8}\left(\frac{1}{C_c^t} + \frac{1}{C_s^t}\right) T_s + \frac{1}{R_1^e} \\
& \left. + \frac{1}{R_1^e} - \frac{\kappa_1 \kappa_3}{4}\left(\frac{1}{C_c^t} + \frac{1}{C_s^t}\right)\right) I - \frac{\kappa_1 T_f}{C_s^t R_f^t} \frac{-\kappa_2 \kappa_3}{R_s^e C_n^e}
\end{aligned} \tag{8}$$

$$\dot{Z} = -\frac{1}{R_s C_n}\left(V_0 + V_1 + V_2 - \kappa_1 \frac{T_c + T_s}{2} - \kappa_2 Z - \kappa_3\right) \tag{9}$$

$$\dot{T}_c = -\frac{V_0}{2C_c^t} - \kappa_1 \frac{I(T_c + T_s)}{2C_c^t} + \kappa_2 \frac{IZ}{2C_c^t} + \kappa_3 \frac{I}{2C_c^t} + \frac{T_s - T_c}{R_c^t C_c^t} \tag{10}$$

$$\dot{T}_s = -\frac{V_0}{2C_s^t} - \kappa_1 \frac{I(T_c + T_s)}{2C_s^t} + \kappa_2 \frac{IZ}{2C_s^t} + \kappa_3 \frac{I}{2C_s^t} + \frac{(T_f - T_s)}{R_f^t C_s^t} + \frac{T_c - T_s}{R_c^t C_s^t} \tag{11}$$

2.2. Model parametrization and experimentation

A series of electrochemical tests were conducted to determine the parameters of the CECM model and to evaluate the performance of the observer. Particularly, the continuous low rate and the intermittent pulse-relaxation (dis)charge were used to measure the OCV function and RC parameters, respectively. All the tests were carried out inside an explosion-proof climate chamber (ESPEC LU-114) at 5, 15, 25 and 35 $^\circ C$ using a NEWARE CT-8008-5V60A-NTFA battery cycler. For the OCV measurement, the cell was first brought to its 100 % SOC using a continuous constant-current (CC) step at 0.05C followed by a constant-voltage (CV) step with a current cutoff limit of 0.02C. The cell was then left at rest for 5 h to achieve a steady state. The cell was then discharged with a CC step of 0.02C and the cutoff voltage limit of 3 V. The voltage-capacity data recorded during this discharge step was utilized as the OCV of the cell (Fig. 2a). In a pulse relaxation test, starting from a fully charged cell, a discharge CC pulse of 0.2C is applied for a duration of 10 min, and then the current is interrupted for a sufficient amount of time until a steady state is reached indicated by a voltage difference between two consecutive readings of <2 mV (Fig. 2b). The ohmic resistance of the cell was calculated as the ratio between the instantaneous voltage right after current interruption and the current value (Fig. 3a). The RC circuit's parameters (Fig. 3b–e) were determined by fitting the voltage profile of each relaxation interval to the following equation:

$$V_0(t) = E_0 - R_1^e exp\left(-\frac{t}{R_1^e C_1^e}\right) - R_2^e exp\left(-\frac{t}{R_2^e C_2^e}\right) \tag{12}$$

To circumvent the computational challenges, a weighted average method was employed to account for the individual thermal contributions from each of the 53 anode and cathode layers. This weighted average method calculates an effective set of parameters that accurately reflects the overall thermal behavior of the cell. The weight coefficients are assigned to each layer commensurate with their volume fraction in the cell. Consequently, the thermal model's parameters set (m_{bat}), which particularly includes the specific heat capacity (c_{bat}^t), density (ρ_{bat}) and thermal conductivity (k_{bat}^t) are calculated according to [41]

$$m_{bat} = \frac{\sum L_i m_i}{L_{bat}} \tag{13}$$

where L_i is the thickness of different layers of the battery and L_{bat} is the battery's thickness and is equal to the $\sum L_i$, as reported in Table B2 in the Appendix B. In this regard, the fraction $\frac{L_i}{L_{bat}}$ in Eq. (13) represents the thermal weight coefficient of the ith layer. The thermal parameters were obtained from the literature reporting the experimental data of the cells similar to the one used in the present study. The detailed information about the chemistry and internal composition of the pouch cell used in this work can be found in our recent publication [42]. It is noteworthy that the $C_c^t = C_s^t = 0.5 c_{bat}^t \rho_{bat} L_{bat} A_{bat}$ and $R_c^t = L_{bat}/k_{bat}^t A_{bat}$.

3. Observer design and stability proof

Considering $x(t) = [V_0 \quad V_1 \quad V_2 \quad Z \quad T_c \quad T_s]$, $y(t) = [V_0 \quad T_s]$, and $u(t) = I(t)$, as a state vector, output, and input of the state space, respectively, the CECM can be expressed as follows:

$$\begin{aligned}\dot{x} &= Ax + Bu + G(x,u,t)\\ y &= Cx\end{aligned} \tag{14}$$

where $A \in R^{6\times6}$ is the system matrix, $B \in R^{6\times1}$ is the input coefficient vector and $C \in R^{2\times6}$is the vector of the output coefficients as following

$$A = \begin{bmatrix} -\kappa_2/R_s^eC_n^e & 1/R_1^eC_1^e - \kappa_2/R_s^eC_n^e & 1/R_2^eC_2^e - \kappa_2/R_s^eC_n^e & {\kappa_2}^2/R_s^eC_n^e & \frac{\kappa_1\kappa_2}{2R_s^eC_n^e} - \frac{\kappa_1}{2R_c^t}\left(1/C_c^t - 1/C_s^t\right) & \frac{\kappa_1\kappa_2}{2R_s^eC_n^e} - \frac{\kappa_1}{2}\left(\frac{1}{R_c^tC_c^t} - \frac{1}{R_c^tC_s^t} + \frac{1}{R_f^tC_s^t}\right)\\ 0 & -1/R_1^eC_1^e & 0 & 0 & 0 & 0\\ 0 & 0 & -1/R_2^eC_2^e & 0 & 0 & 0\\ 1/R_s^eC_n^e & 1/R_s^eC_n^e & 1/R_s^eC_n^e & -\kappa_2/R_s^eC_n^e & -\kappa_1/2R_s^eC_n^e & -\kappa_1/2R_s^eC_n^e\\ -1/2C_c^t & 0 & 0 & 0 & -1/R_c^tC_c^t & 1/R_c^tC_c^t\\ -1/2C_c^t & 0 & 0 & 0 & 1/R_c^tC_c^t & -1/R_c^tC_c^t - 1/R_f^tC_c^t \end{bmatrix} \tag{15}$$

$$B = \begin{bmatrix} 1/R_1^e + 1/R_1^e - \frac{\kappa_1\kappa_3}{4}\left(1/C_c^t + 1/C_s^t\right)\\ 1/C_1^e\\ 1/C_2^e\\ 0\\ \kappa_3/2C_c^t\\ \kappa_3/2C_s^t \end{bmatrix} \tag{16}$$

$$G(x,u) = \begin{bmatrix} \left(-\frac{\kappa_1}{4}\left(\frac{1}{C_c^t} + \frac{1}{C_s^t}\right)\left(V_0 - \kappa_2 Z - \frac{\kappa_1}{2}(T_c + T_s)\right)\right)I\\ 0\\ 0\\ -\kappa_3/R_s^eC_n^e\\ -\kappa_1\frac{I(T_c+T_s)}{2C_c^t} + \kappa_2\frac{IZ}{2C_c^t} + \kappa_3\frac{I}{2C_c^t}\\ -\kappa_1\frac{I(T_c+T_s)}{2C_s^t} + \kappa_2\frac{IZ}{2C_s^t} + \kappa_3\frac{I}{2C_s^t} + \frac{T_f}{R_f^tC_s^t} \end{bmatrix} \tag{17}$$

In Eq. (14), $G(x,u) \in R^{6\times1}$ represents the nonlinear part of the model and it can be assumed that

$$G(x,u) = \Gamma\xi(x,u,t) \tag{18}$$

where $\Gamma \in R^{6\times1}$ is the model nonlinear input matrix and $\xi(x,u,t) \in R^{(1\times1)}$ is an unknown and bounded function as follows

$$\|\xi(x,u,t)\| \le \psi \forall x \in R^{6\times1}, u \in R^{1\times1} \text{ and } t \ge 0 \tag{19}$$

where ψ is a positive constant. To estimate the SOC and internal temperature of the studied battery during discharge, the adaptive gain sliding mode observer is proposed as follows:

$$\dot{\hat{x}} = A\hat{x} + Bu + K(y - C\hat{x}) + v \tag{20}$$

where K is feedback gain and v is an adaptive switching gain function. To guarantee the stability and the robustness of the observer, the switching gain function is considered as a discontinuous sign function as below

$$v = \begin{cases} \hat{\theta}(e_y(t))\Gamma sgn(e_y(t)) & e_y \ne 0\\ 0 & \text{otherwise}\end{cases} \tag{21}$$

where $e_y(t) = y(t) - \hat{y}(t) = C(x - \hat{x}) = Ce(t)$. Here, the state estimation errors are defined as $e = x - \hat{x}$ and adaptive switching gain will be updated by using the following adaptation law

$$\dot{\hat{\theta}}(e_y(t)) = \alpha|e_y(t)| \tag{22}$$

where α is an adaptation constant, and by choosing an appropriate value for it, the adaptation speed can be adjusted. To proceed with stability proof, by subtracting Eqs. (14) and (20) and by defining $A_0 = A - KC$, the dynamics of state estimation can be expressed as

$$\dot{e} = A_0 e + G(x,u,t) - v \tag{23}$$

A Lyapunov function candidate, including estimation and adaptation errors, can be considered as below

$$W\left(e,\tilde{\theta}\right) = \frac{1}{2}e^TPe + \frac{1}{\alpha}\tilde{\theta}^2 \tag{24}$$

where $\tilde{\theta} = \hat{\theta} - \theta_d$ is the adaptation error between the estimated switching gain and the desired one. The time derivative of $W\left(e,\tilde{\theta}\right)$ is acquired as

$$\begin{aligned}\dot{W}(e,\tilde{\theta}) &= \frac{1}{2}\left(\dot{e}^TPe + e^TP\dot{e}\right) + \frac{1}{\alpha}\tilde{\theta}\dot{\theta}\\ &= \frac{1}{2}\left[e^T\left(A_0P + PA_0{}^T\right)e\right] + \frac{1}{2}\left(\left(G^T - v^T\right)Pe + e^TP(G - v)\right) + \frac{1}{\alpha}\tilde{\theta}\dot{\theta}\end{aligned} \tag{25}$$

According to Lyapunov stability, there exists a symmetric definite matrix (P) such that it satisfies the following equation

$$-Q = A_0P + PA_0{}^T \tag{26}$$

where Q is a definite and symmetric positive matrix and the Lyapunov matrices pair (P, Q) for A_0 satisfies a geometrical constraint

$$C = \Gamma^TP \tag{27}$$

Consequently, Eq. (25) can be rearranged as follows

$$\begin{aligned}\dot{W}(e,\tilde{\theta}) &= -\frac{1}{2}\left[e^TQe\right] + \left(\xi(x,u,t)\Gamma^T - v^T\right)Pe + \frac{1}{\alpha}\tilde{\theta}\dot{\theta}\\ &= -\frac{1}{2}\left[e^TQe\right] + \xi Ce - \hat{\theta}(e_y(t))sgn(e_y(t))\Gamma^TPe + \frac{1}{\alpha}\tilde{\theta}\dot{\theta}\\ &= -\frac{1}{2}\left[e^TQe\right] + \xi Ce - \hat{\theta}(e_y(t))sgn(e_y(t))\Gamma^TPe + 2(\hat{\theta} - \theta_d)\alpha|e_y(t)|\\ &= -\frac{1}{2}\left[e^TQe\right] + \left(\xi - \theta_d sgn(e_y(t))\right)e_y(t)\end{aligned} \tag{28}$$

The first term on the right hand of the equation is always negative and the following inequality can be written

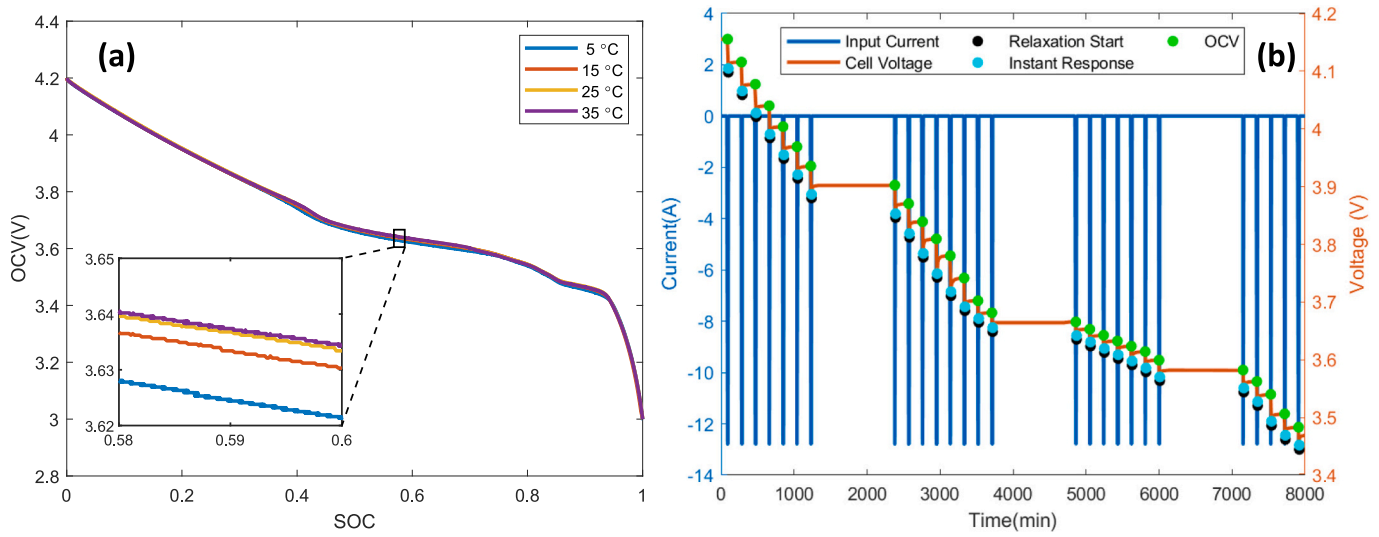

Fig. 2. **(a)** OCV profile of the pristine cell at different temperatures, **(b)** Voltage and current variation for 0.2C pulse-relaxation current and key points for extraction of the CECM's parameters.

$$-\frac{1}{2}e^{T}Qe \leq -\frac{1}{2}\lambda_{min}(Q)\|e\|^{2} \tag{29}$$

where $\lambda_{min}(Q)$ is the smallest eigenvalue of Q. Furthermore, the second term in Eq. (28) is always negative since

$$\left(\xi - \theta_d sgn\left(e_y(t)\right)\right)e_y(t) = \begin{cases} < 0 & : e_y(t) > 0 \quad \theta_d > \psi \\ < 0 & : e_y(t) < 0 \quad \theta_d > \psi \end{cases} \tag{30}$$

As $\|\xi(x,u,t)\| \leq \psi$, there should be a desired finite switching gain θ_d such that $\theta_d > \psi$, leading to $\dot{W}\left(e,\widetilde{\theta}\right) < 0$. Therefore, the second method of the Lyapunov stability is fulfilled, and as a result, asymptotic convergence of state estimation to zero as time tends to infinity is ensured. As the switching gain is adaptively updated in response to estimation error, the proposed adaptive SMO can provide robust performance. However, discontinuity in the sign function of the SMO leads to a chattering effect [29], where, without loss of generality, we consider a continuous switching function as following

$$v = \begin{cases} \widehat{\theta}\left(e_y(t)\right)\Gamma \dfrac{e_y(t)}{\|e_y(t)\| + \delta_v} & e_y \neq 0 \\ 0 & \text{otherwise} \end{cases} \tag{31}$$

The following section will present the experimental and simulation results to validate the proposed adaptive SMO for effectively estimating SOC.

4. Results and discussion

4.1. SOC and temperature effect on ECM parameters

The OCV variation versus SOC is shown for the four temperatures in Fig. 2a. As it is seen, the OCV experiences minimal variation in response to temperature changes. Fig. 2b illustrates the current and terminal voltage profiles during the deep intermittent discharge of the pristine commercial cell at 25 °C with 0.2C pulse-relaxation protocol. The same test was repeated at 5, 15 and 35°C, and the key points from the voltage response profiles of the cell (Fig. 2b) were used to parametrize the CECM.

The obtained parameters were used to construct and implement the CECM as a nonlinear model in the Simulink. The ECM model was parameterized for a discrete set of SOC and temperature levels (Fig. 3). The ECM parameters for the points lying in-between these finite set of temperature and SOC values were obtained by a linear interpolation during the implementation of the ECM in the Simulink software. However, in the stage of observer design, the possible variations of the ECM parameters for the internal points were ignored within each SOC interval. This simplifying assumption reduces the complexity and computational expense of the observer and enhances the feasibility of proving the convergence stability of the observer.

Prior to the observer design, the performance of the ECM model was rigorously evaluated by contrasting the simulation outputs against experimental discharge data. To this end, a fully charged cell was isothermally discharged at 25 °C with intermittent 0.2C current pulses (10 min) and relaxation intervals of 120 min (Fig. 4). The experimental SOC values ('Exp' legend in Fig. 4) were obtained by the coulomb counting of the discharge process. On the other hand, within the ECM model, the SOC is a state variable and can be calculated as a function of time by solving the corresponding initial value problem defined by the ordinary differential equations of the ECM model. The comparison of the experiment and simulation confirms the promising performance of the ECM model (Fig. 4).

4.2. Observability of the design model

Before presenting the performance of the adaptive observer, it is crucial to assess the observability of the design model. In the case of a linear component, determining the rank of the observability matrix for matrices A and C can be done as follows [24]

$$O_b(A,C) = \begin{bmatrix} C \\ CA \\ \vdots \\ CA^5 \end{bmatrix} \tag{32}$$

Rank of the $O_b(A,C)$ matrix was calculated and the results show that the matrix is not full rank (Fig. C1) which implies a linear correlation among the rows or columns. This means that some states of the system are not uniquely determined by the available measurements, and therefore cannot be fully observed or estimated. Nevertheless, by taking the nonlinear part into account, the following matrix should be calculated and added to $O_b(AC)$ matrix [29]

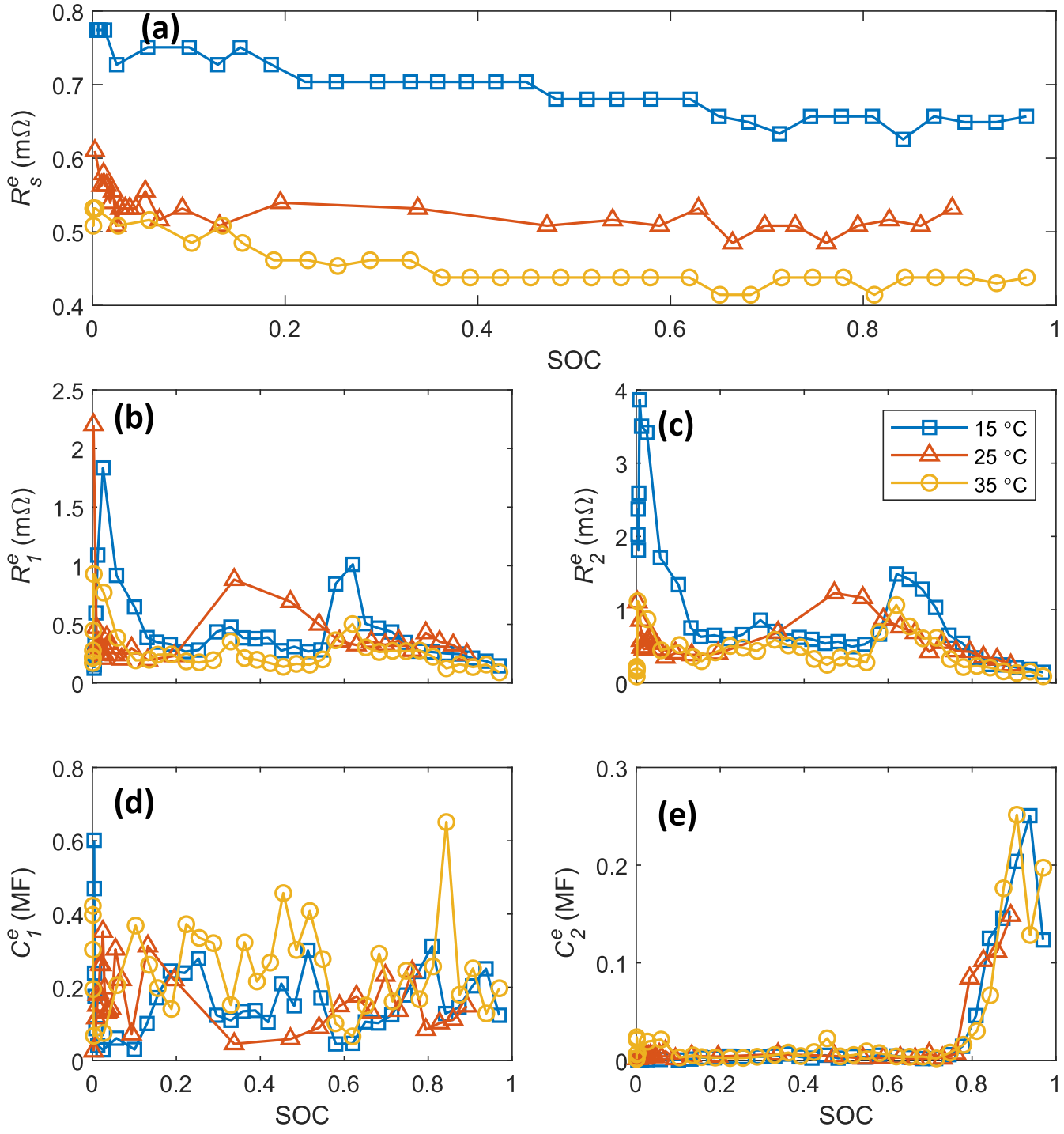

Fig. 3. Extracted CECM parameters **(a)** R_s^e, **(b)** R_1^e, **(c)** R_2^e, **(d)** C_1^e and **(e)** C_2^e by using pulse-relaxation response of the pristine cell at different temperatures.

$$O_b(G,C)=\begin{bmatrix} L_G^0(Cx) \\ L_G^1(Cx) \\ \vdots \\ L_G^5(Cx) \end{bmatrix} \tag{33}$$

where $L_G^i(Cx)$ is i^{th} Lie derivative [24] of outputs ($y = Cx$) with respect to G. For instance, $L_G^1(Cx)$ is defined as follows:

$$L_G^1(Cx)=\nabla(Cx).G=\begin{bmatrix} \frac{\partial Cx}{\partial x(1)} & \frac{\partial Cx}{\partial x(2)} & \frac{\partial Cx}{\partial x(3)} & \frac{\partial Cx}{\partial x(4)} & \frac{\partial Cx}{\partial x(5)} & \frac{\partial Cx}{\partial x(6)} \end{bmatrix} G=\begin{bmatrix} 1 & 0 & 0 & 0 & 0 & 0 \\ 0 & 0 & 0 & 0 & 0 & 1 \end{bmatrix}$$

$$\begin{bmatrix} \left(-\frac{\kappa_1}{4}\left(\frac{1}{C_c^t}+\frac{1}{C_s^t}\right)\left(V_0-\kappa_2 Z-\frac{\kappa_1}{2}(T_c+T_s)\right)\right)I \\ 0 \\ 0 \\ -\kappa_3/R_s^e C_n^e \\ -\kappa_1\frac{I(T_c+T_s)}{2C_c^t}+\kappa_2\frac{IZ}{2C_c^t}+\kappa_3\frac{I}{2C_c^t} \\ -\kappa_1\frac{I(T_c+T_s)}{2C_s^t}+\kappa_2\frac{IZ}{2C_s^t}+\kappa_3\frac{I}{2C_s^t}+\frac{T_f}{R_f^t C_s^t} \end{bmatrix} \tag{34}$$

The CECM becomes observable by using the higher-order Lie derivative on the coupled system (Fig. C1). It is noteworthy that the inclusion of two nodes in the thermal model is beneficial in two respects. First, ignoring the heat generation at the surface node results in an observability matrix that is not full-rank, which in turn prevents the observer from establishing a mathematical relationship between surface temperature and SOC. Second, a thermal model with more than one node provides a more representative physical picture of a thick pouch cell with 53 layers of cathodes and anodes in which the possible non-uniform generation and distribution of heat cannot be ignored.

4.3. Observer performance

4.3.1. Observer evaluation by simulation

In this section, the performance of the adaptive observer will be presented at various conditions. The feedback gain matrix (K) and switching gain constant (Γ) are attained by optimising the summation of mean absolute error (MAE) for voltage, surface temperature, and SOC during a 1C pulse relaxation discharge using the fminsearch method:

$$K=\begin{bmatrix} 0.45 & -0.002 & 0.007 & 0.004 & -0.001 & -0.002 \\ -0.001 & 0.000 & -0.001 & -0.004 & -0.000 & 0.198 \end{bmatrix}^T \tag{35}$$

$$\Gamma=\begin{bmatrix} 4.8 & 0 & 0 & 0 & 0 & 0 \\ 0 & 0 & 0 & 0 & 0 & 4.1 \end{bmatrix}^T \tag{36}$$

It is worth mentioning that error signals are scaled using their initial values to equalize their contribution to the objective function. The positive constant α is chosen as 5×10^{-3} to satisfy the adaptation speed for the switching gains function. The adaptation constant impacts the two main aspects of the observer's performance: convergence speed and noise robustness. Increasing α accelerates convergence but potentially makes the observer less robust to the noise. Conversely, decreasing α decelerates the convergence but improves the noise robustness. Here, the optimal value of α was fine tuned via a trial and error procedure starting from the available values reported for the similar systems in the literature (see references [21, 33]) to achieve a satisfactory balance between the convergence speed and noise robustness. Also, the initial values of the observer were selected with 10 % deviation from the design model ones. The ode23tb solver was employed to solve the initial value equations to overcome discontinuities aroused from the input signals and sign function. Detailed information about the simulation methods in the Simulink of the MATLAB software is provided in the Appendix (Table D1). To clarify the structure of the observer, Fig. C2 in the Appendix represents a flowchart of the proposed observer.

First, the pulse relaxation test with constant current was used to evaluate the observer's robustness in handling deviations in the initial guess. The simulation involved deviating the initial values of the adaptive observer by 5 %, 10 %, and 20 % relative to the design model. The results show that unlike the available observers in the literature [43,44] the proposed observer of the present study can overcome initial condition mismatch and accurately estimate the design model outputs

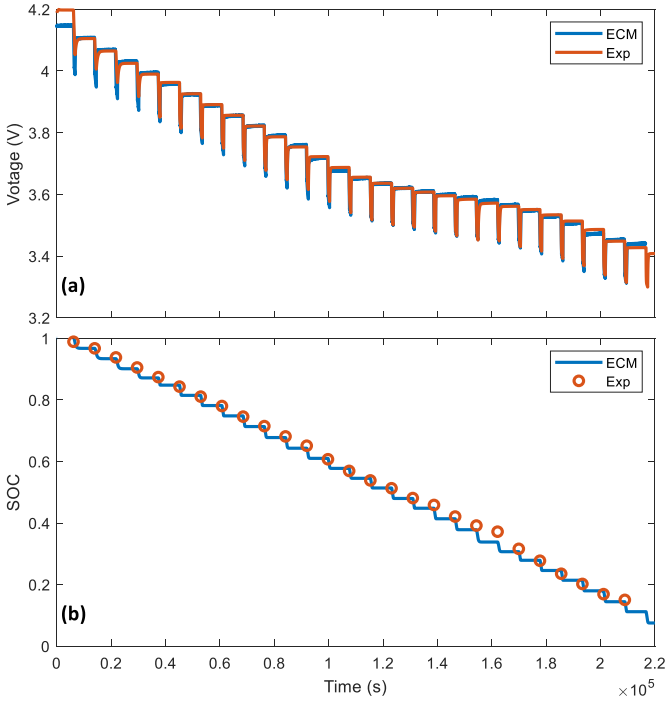

Fig. 4. Performance of the design model in simulating the experimental profiles of **(a)** voltage and **(b)** SOC during a deep intermittent discharge of the pristine cell with 0.2C current pulses of 10 min duration and 120 min relaxation periods at 25 °C.

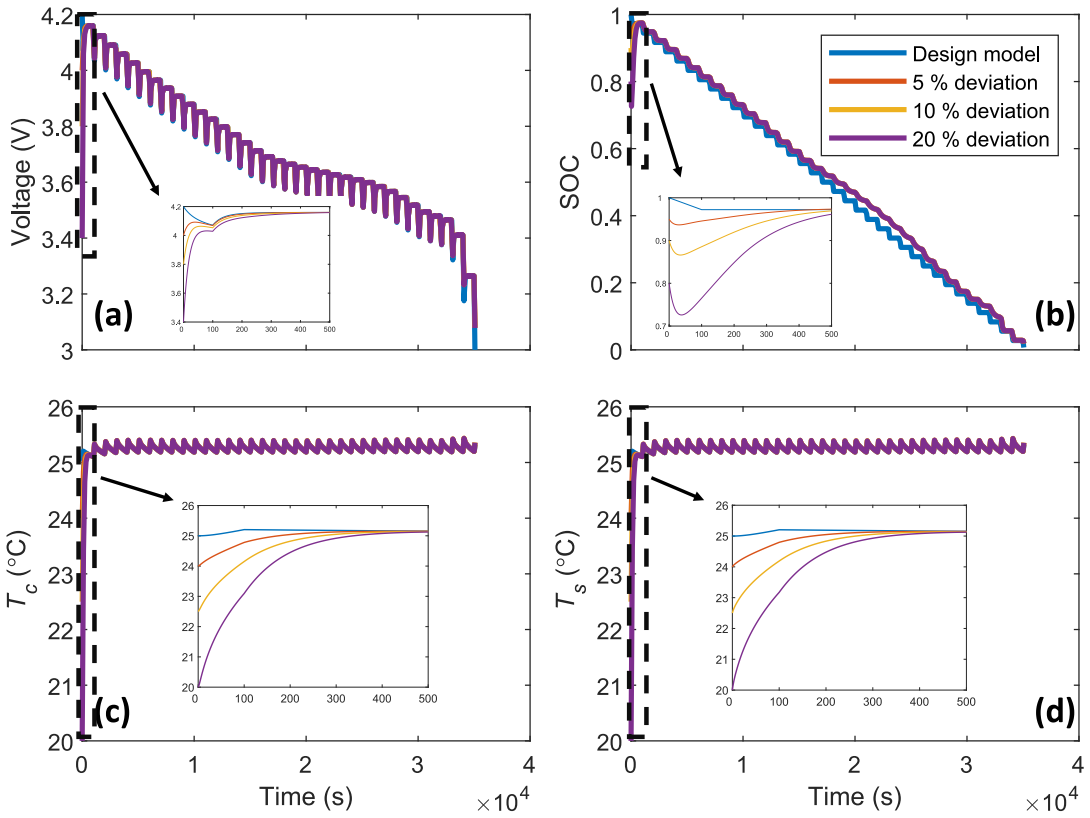

Fig. 5. Observer performance in estimation of output and internal states of the design model and its robustness to initial condition under pulse-relaxation current: **(a)** V_0, **(b)** SOC, **(c)** T_c and **(d)** T_s.

and internal states (Fig. 5). The observer converges for all the states within almost 300 s. This rapid convergence is attributed to the observer's simultaneous utilization of voltage and temperature errors for the estimations' correction, an advantage over decoupled observer designs that treat voltage and temperature separately [45]. Furthermore, the estimation error indicates that the observer can effectively avoid chattering. The estimation error for voltage is $<$10 mV for almost the entire simulation period. Still, it exceeds this bound for the last three impulses due to the abrupt change in voltage and its higher sensitivity to changes in current. Nonetheless, the observer can reduce the estimation error within a short period. The SOC and temperature errors fall within the bounds of 0.05 and 0.05 $^{\circ}C$, respectively, demonstrating the robust capability of the proposed observer (see Fig. C3 in the Appendix).

In the next step, the design model and observer were subjected to urban dynamometer driving schedule (UDDS) current profile (see Fig. C4 in Appendix) to assess the performance of the proposed observer under more realistic conditions that more closely resemble real-world driving behavior compared to the idealized pulse-relaxation current profile. Additionally, a random initial state ([4.5 0 0 0.5 20 20]) was selected for the observer. This was done to prevent the observer from imitating the design model's internal states instead of estimating them. The estimation results are compared against the actual values in Fig. 6 suggesting that the proposed observer adeptly tracks the measured voltage and surface temperature of the design model (Fig. 6a, d). Moreover, the observer estimates the internal states of the design model relatively efficiently and robustly, with MAE for SOC and core temperature of 0.0272 and 0.0347 $^{\circ}C$, respectively. The observer quickly reduces the SOC estimation error from 0.5 to a bound of $(-0.05, 0.05)$ and keeps the error within this bound for the rest of the simulation (Fig. 6b). There is a small difference (0.5 $^{\circ}C$) between surface and core temperature implying a relatively uniform temperature distribution within the cell (Fig. 6c–d). This is not surprising for the commercial battery investigated here with a large heat transfer area and is in line with the reported temperature variations in similar batteries [46,47]. Moreover, here, the battery is cooled within a thermal chamber with a natural convection which has been shown to result in a more uniform temperature distribution compared to the forced convection cooling [48]. In the thermal model of the present study, the heat generation term was not limited to the core and was also considered for the surface node. This ensures not only the observability of the design model but also a more realistic thermal picture of the cell. In this regard, the possibility of heat generation at the surface node can potentially better simulate the circumstances in which a more uniform temperature distribution is expected. As a further assessment of the proposed observer, a comparative evaluation was conducted with the existing adaptive gain SMOs from literature (ref. [21, 33]) in estimation of the battery SOC when loaded with a UDDS current profile (Fig. C5 in Appendix C). It is important to highlight that the adaptive gain observers from ref. 21 and 33 struggled when confronted with a significant deviation from the initial design model parameters. Therefore, an initial state vector of [4.5 0 0 0.8] was used for the comparative investigation. The analysis clearly reveals that the observer designed using the CEMC exhibits outstanding performance in the estimation of SOC with a MAE of 0.022 compared to 0.028 and 0.027 with observers of ref. 21 and 33, respectively.

4.3.2. *State estimations against experiments*

The practical merits of the designed observer was evaluated by comparing its prediction outputs with the experimental data from a commercial 64 Ah Li-ion pouch cell at the pristine and aged conditions (Fig. 1 a,d). The target task for the observer was to estimate the SOC and core temperature of the pouch cell during a deep constant-current discharge at 0.8C starting from a fully charged state. To obtain the true values of SOC, the cell was discharged stepwise with the current pulses of 0.8C lasting for 30 min each. The current had to be interrupted intermittently during the cell discharge to allow the relaxation of the voltage towards equilibrium. The voltage at the end of each relaxation

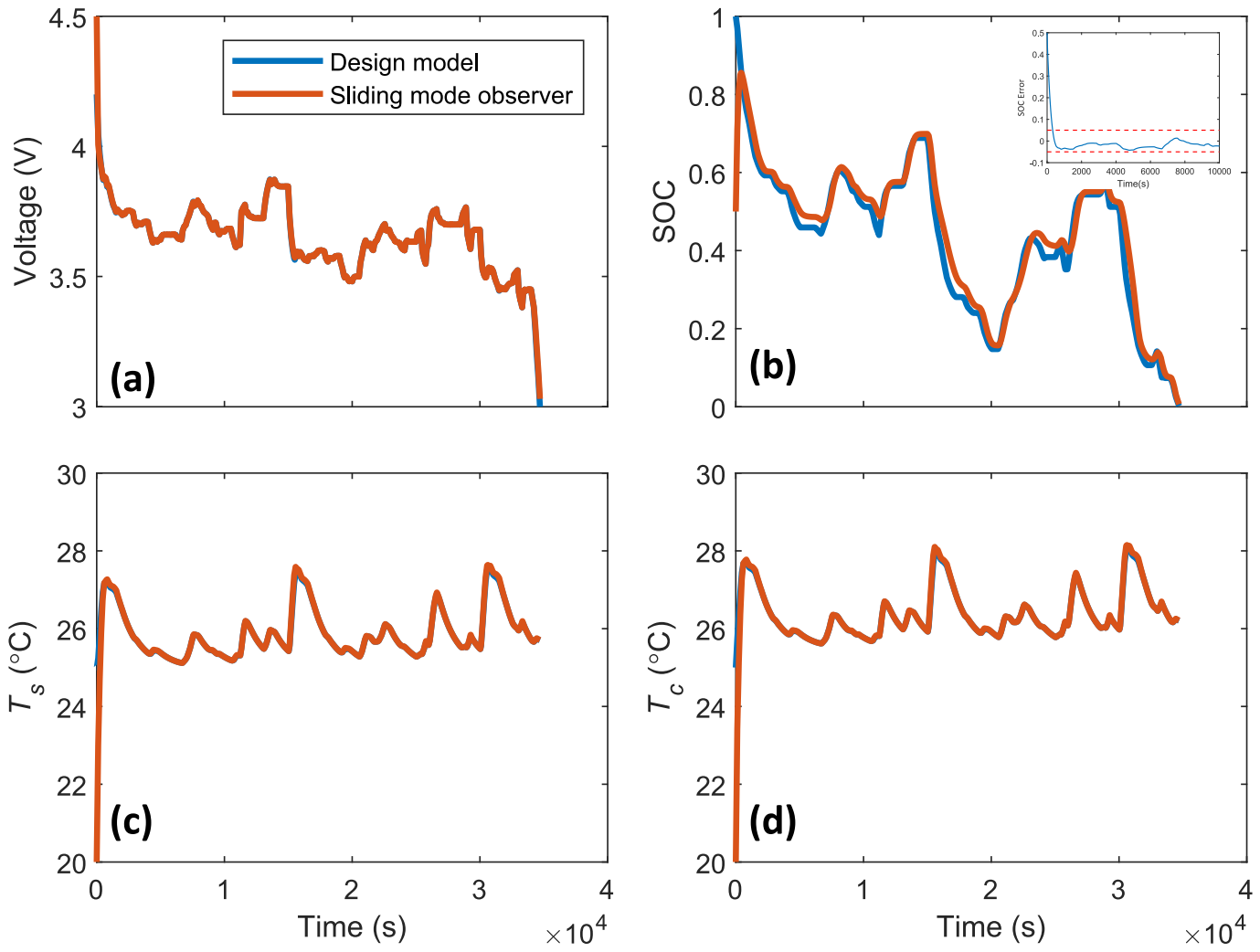

Fig. 6. Evaluation of observer accuracy in predicting the design model's output and state variables using the UDDS current profile **(a)** V_0, **(b)** SOC, **(c)** T_s and **(d)** T_c.

period (6–7 h) was considered to be the OCV which provides an accurate SOC reading to be compared with the observer predictions. The current, voltage, and temperature profiles during each current pulse period were fed as the input to the observer for state estimations (Fig. 1c).

The observer's predictions closely follow the experimental data during the whole period of deep discharge for the pristine Li-ion pouch cell (Fig. 7). The temperature profile shows some fluctuations induced by the noise in the surface temperature measurements. Noteworthy is the accurate predictions of the SOC by the observer confirmed by the experimental values of the SOC (circle blue markers in Fig. 7c). At the end of each current-pulse period, the experimental SOC was determined by averaging the cell voltage over the last 10 min of the subsequent relaxation period and after consulting the experimental OCV function of the cell (Eq. A4, Appendix).

The proposed observer of this study was parametrized based on a pristine pouch cell and therefore its predictions are expected to deviate from the true states for the aged cells. It is, however, still interesting to evaluate the performance of the observer when confronted with the same cell but at a state-of-health (SOH) below 100 %. To do so, the same experimental discharge protocol (Fig. 7a) was applied to the other two aged batteries with the SOH values of 99 % and 93 %. The observer's performance in estimating the SOC for these aged batteries is summarized in Fig. 8. The estimation error is negligible for the cell with SOH = 99 % (Fig. 8a), but as high as 8 % and 6 % at SOC = 40 % and SOC = 15 %, respectively, for the cell with SOH = 93 % (Fig. 8b). This is not surprising since the internal resistances and OCV function of the cell are subject to the variations in the presence of aging. Particularly, the OCV function of a Li-ion battery is very sensitive to the relative positioning of the individual OCVs of the cathode and anode electrodes made thereof. This relative positioning (i.e. cell balancing) is known to change due to the loss of lithium and/or active-material in either of the electrodes. Such evolutions in the cell parameters need to be accounted for in designing an observer suitable for the whole lifetime of the cell which is the subject of future works.

5. Conclusion

This paper introduced an enhanced sliding mode observer (SMO) for the robust and immediate estimation of the State of Charge (SOC) and internal temperature of the lithium-ion batteries (LIBs). The proposed SMO benefits from an adaptive law to adjust the switching gain which is enabled by a coupled equivalent circuit model (CECM) representing the electrochemical and thermal behavior of the battery. This adaptive feature enhanced the robustness of the observer against the uncertainties in the model parameters and disturbances in the measurements. The performance of the proposed SMO was rigorously evaluated through a combination of simulations and experiments. Results demonstrated the remarkable accuracy of the SMO in estimating the SOC and internal temperature even under complex load profiles such as pulse relaxation and UDDS. The observer proved resilient to initial guess deviations and significant model mismatches, effectively mitigating the chattering effect. In this regard, the role of the continuous switching and

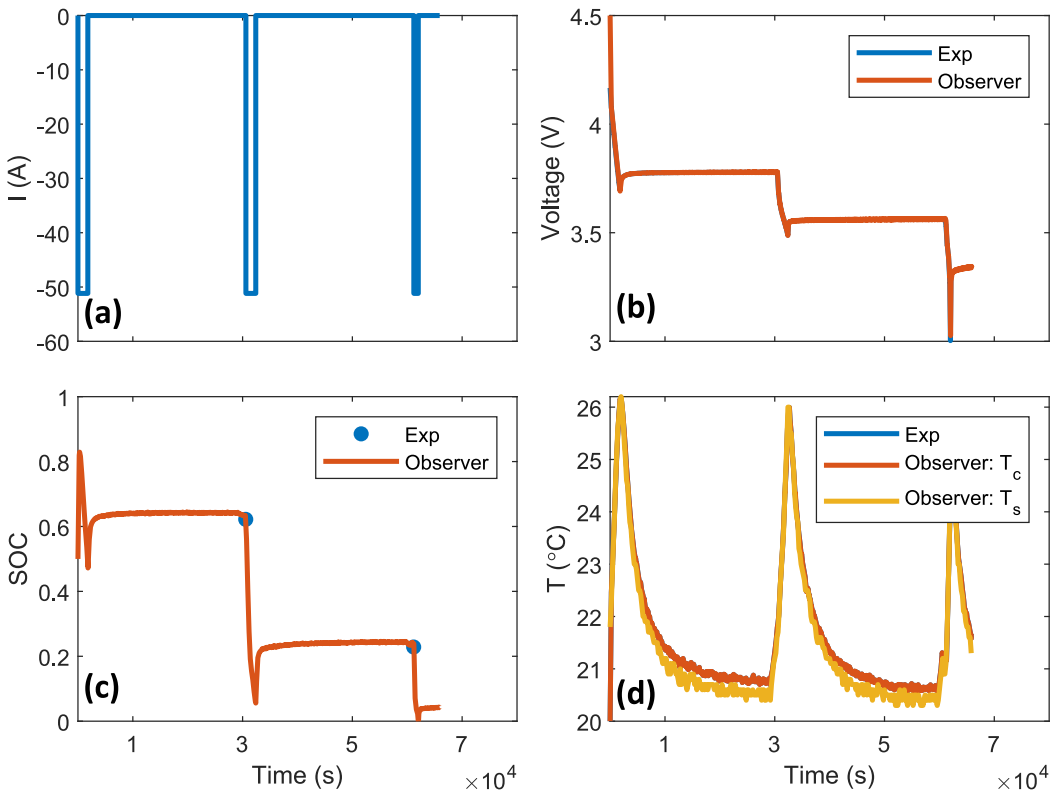

Fig. 7. The experimental (blue solid line and circle markers) and prediction profiles (brown and red) of **(a)** the current, **(b)** Voltage, **(c)** SOC, and **(d)** internal and surface temperature during the deep discharge of the pristine Li-ion pouch cell with current pulses of 0.8C (30 min) and intermittent relaxation periods of 6–7 h. (For interpretation of the references to color in this figure legend, the reader is referred to the web version of this article.)

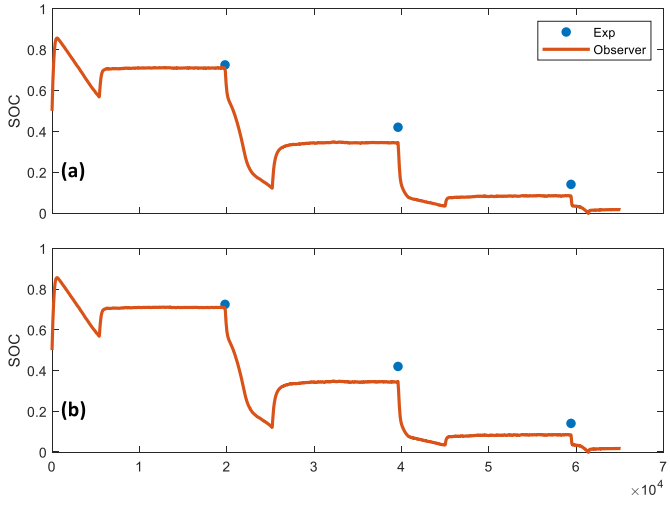

Fig. 8. The experimental (blue circle markers) and predicted SOC (brown and red) compared for two Li-ion pouch cell with **(a)** SOH = 99 % and **(b)** SOH = 93 % during the deep discharge with current pulses of 0.8C (30 min) and intermittent relaxation periods of 6–7 h. (For interpretation of the references to color in this figure legend, the reader is referred to the web version of this article.)

adaptive gain features of the observer are noteworthy. The continuous switching enables a smooth transition between the states and hence avoids the abrupt changes that can otherwise promote chattering. The adaptive gain adjusts the system's gain in real-time according to the current state and the error measurements. This adaptability ensures that the gain is high enough to maintain a robust control but not so high as to produce unnecessary chattering.

The performance of the observer was investigated with experimentation on a commercial 64 Ah LIB cell at both pristine and aged conditions. Remarkably, the observer achieved SOC estimates with <1 % and 3 % error for the fresh and aged cells, respectively. In summary, the proposed SMO is showcased to be a promising tool for estimating the SOC and internal temperature of the LIBs. This SMO has a potential application in battery management systems to enhance the performance and safety of the LIB-powered devices.

Nomenclature

Abbreviations

ANFIS	adaptive neuro-fuzzy inference system
ANN	artificial neural networks
CC	constant current
CECM	coupled equivalent circuit model
CV	constant voltage
ECM	equivalent circuit model
EKF	extended Kalman filter
KF	Kalman filter
LIBs	lithium-ion batteries
MAE	mean absolute error
OCV	open circuit voltage (V)
P2D	psuedo-2-dimensional
PIO	proportional integral observer
sgn	sign function
SMO	sliding mode observer
SOC	state of charge
SVM	support vector machines
UDDS	urban dynamometer driving schedule
UKF	unscented Kalman filter

Variables

A	system matrix
B	input coefficient vector
C	output coefficient vector
C_1^e	first RC branch capacitance (F)
C_2^e	second RC branch capacitance (F)
C_n^e	battery capacity (Ah)
C_c^t	heat capacity of the core (J/°C)
C_s^t	heat capacity of the surface (J/°C)
c_{bat}^t	specific heat capacity of the surface (J/kg/°C)
e	estimation error of states
E_0	OCV (V)
e_y	estimation error of outputs
F	Faraday constant (sA/mol)
G	model nonlinear part
I	current (A)
k^t	thermal conductivity (J/sm°C)
K	feedback gain
L^i	i^{th} lie derivative
L_{bat}	battery thickness (μm)
L_i	thickness of battery layers (μm)
m_{bat}	thermal model parameters for battery
m_i	thermal parameters for layer 'i'
O_b	observability matrix
P	symmetric definite matrix
Q	symmetric definite matrix
R_1^e	first RC branch resistance (Ω)
R_2^e	second RC branch resistance (Ω)
R_c^t	conduction thermal resistance inside the battery (s°C/J)
R_f^t	convection thermal resistance outside the battery (s°C/J)
R_s^e	internal ohmic resistance of the battery (Ω)
T_c	core temperature (°C)
T_f	ambient temperature (°C)
T_s	surface temperature (°C)
u	system inputs
v	adaptive switching gain function
V_0	cell voltage (V)
V_1	polarization voltage (V)
V_2	polarization voltage (V)
W	Lyaponov function
x	states vector
y	outputs vector
Z	SOC
Z_0	initial SOC
α	adaptation constant
δ_v	estimation error criterion
Γ	nonlinear input matrix
κ_1	OCV derivative to temperature (V/°C)
κ_2	OCV derivative to SOC (V)
κ_3	OCV bias (V)
ξ	unknown function of design model
ψ	upper bound of unknown function ξ
λ	Eigenvalue
φ	bound of the nonlinear part
ρ	density (kg/m^3)
θ_d	desired adaptive switching gain
$\widehat{\theta}$	estimated adaptive switching gain
$\widetilde{\theta}$	error of adaptive switching gain
ΔS	entropy change of overall electrochemical reaction (V/°C)

CRediT authorship contribution statement

Behnam Ghalami Choobar: Writing – review & editing, Writing – original draft, Visualization, Software, Methodology, Investigation, Conceptualization. **Hamid Hamed:** Writing – review & editing, Visualization, Validation, Methodology, Investigation. **Mohammadhosein Safari:** Writing – review & editing, Visualization, Supervision, Resources, Methodology, Funding acquisition.

Declaration of competing interest

No conflict of interest.

Data availability

Data will be made available on request.

Acknowledgments

This work was supported by funding from the European Union's Horizon 2020 research and innovation program for the Current Direct project under grant agreement No.963603.

Appendix A. Thermal model

The paper employs a design model for the prismatic batteries that consists of two sub-models: an electrical model and a thermal model. The electrical model is based on an equivalent circuit that relates the current (I) and the terminal voltage (V_0) of the battery. The thermal model has two states: the surface temperature (T_s) and the core temperature (T_c) of the battery. The model assumes that the temperature only can vary across the thickness of the pouch cell, which simplifies the calculations and reduces the computational time.

The battery is discretized into two nodes of surface and core to which the following general energy balance is applied to derive the thermal model:

$$\dot{Q}_{acc} = \dot{Q}_{gen} + \dot{Q}_{in} - \dot{Q}_{out} \tag{A1}$$

where $\dot{Q}_{acc}$ is the accumulation rate of the thermal energy, $\dot{Q}_{gen}$is the rate of internal heat generation, and $\dot{Q}_{in}$ and $\dot{Q}_{out}$ are the rate of heat influx and outflux, respectively. The accumulation rate of energy in each node is explained by: $\dot{Q}_{acc} = C^t\frac{dT}{dt}$, in which the heat capacity (C^t) is considered to be different for the surface (C_s^t) and core (C_c^t) of the battery.

The rate of heat transfer between the nodes and the surface node and the surroundings can be expressed by $\dot{Q} = \Delta T/_{R^t}$ in which ΔT and R^t is the temperature difference and the heat transfer resistance, respectively. The heat transfer resistance for the convection and conduction modes are described with $R^t = 1/hA$ and $R^t = l/k^tA$, respectively, where h is the convective heat transfer coefficient, A is the surface area, l is the thickness, and k^t is the thermal conductivity.

The rate of internal heat generation consists of two parts: reversible ($\dot{Q}_{gen}^{Rev}$) and irreversible ($\dot{Q}_{gen}^{Ire}$). The reversible part is related to the change in the entropy (ΔS) of the overall redox reaction of the cell and can be expressed as $\dot{Q}_{gen}^{Rev} = IT\Delta S/F$. The irreversible part is caused by the deviation of the the terminal voltage (V_0) from the open circuit voltage (E_0) of the cell and can be written as $\dot{Q}_{gen}^{Ire} = I(E_0 - V_0)$.

The resulting thermal model consists of the following two equations describing the dynamics of temperature variation for the surface and core nodes of the battery:

$$\dot{T}_c = \frac{I(E_0 - V_0)}{2C_c^t} - \frac{I(T_c + T_s)\Delta S}{2FC_c^t} + \frac{T_s - T_c}{R_c^t C_c^t} \tag{A2}$$

$$\dot{T}_s = \frac{I(E_0 - V_0)}{2C_s^t} - \frac{I(T_c + T_s)\Delta S}{2FC_s^t} + \frac{T_c - T_s}{R_c^t C_s^t} + \frac{(T_f - T_s)}{R_f^t C_s^t} \tag{A3}$$

Appendix B. Battery cell characteristics

In the present study, a lithium-ion pouch cell with a nominal capacity of 64 to 67.5 ampere-hours (Ah) was experimented. This cell weighs ~1156.2 g and measures approximately $100.2 \pm 1.5 \times 352.2 \pm 1 \times 16.1 \pm 0.1$ mm. The cell stack consists of 52 layers of NMC cathode and 53 layers of graphite anode zig-zag stacked with separator in between. Our recent paper reports a detailed teardown analysis of this cell [42]. The open-circuit voltage (OCV) of the cell, as experimentally determined, is documented in Table B1. Additionally, Table B1 presents the physical characteristics of the cell used in the model, including the electrode and current collector thicknesses, as well as cell area. Other properties listed in Table B2 were sourced from the available literature investigating the similar Li-ion cells.

OCV analytic equation for pristine cell

$$f(x) = p_1x^9 + p_2x^8 + p_3x^7 + p_4x^6 + p_5x^5 + p_6x^4 + p_7x^3 + p_8x^2 + p_9x + p_{10} \tag{B4}$$

where the coefficient and 95 % confidence intervals are reported in Table B1.

Table B1
Coefficients and 95 % confidence intervals of Eq. B4.

	Value	Lower	Upper
p_1	−0.0177	−0.018	−0.0175
p_2	−0.03	−0.0303	−0.0298
p_3	0.0884	0.0866	0.0902
p_4	0.1545	0.1531	0.1559
p_5	−0.1413	−0.1453	−0.1374
p_6	−0.2752	−0.2777	−0.2727
p_7	0.0524	0.0491	0.0557
p_8	0.2235	0.2219	0.225
p_9	−0.1791	−0.18	−0.1783
p_{10}	3.6692	3.6690	3.6694

Table B2
Specifications of the cell and obtained parameters for the thermal model.

Property	Battery	Copper Collector (ref. [49])	Anode (Graphite) (ref. [50, 51])	Separator (ref. [50])	Cathode (NMC 111) (ref. [50, 51])	Aluminum collector (ref. [49])
Thermal conductivity ($\frac{W}{m^\circ C}$)	35	385	1	0.5	3.6	238
Density (kg/m^3)	3375	8960	2300	913	4870	2700
Specific capacity ($\frac{J}{kg^\circ C}$)	1055	385	750	2480	840	900
Length (μm)	146	10	59	25	48	4
Area (cm^2)	650					
Heat capacity ($\frac{J}{^\circ C}$)	1800					
Thermal conductive resistance ($\frac{^\circ C}{W}$)	15.6					

Appendix C. Supplementary data

Supplementary data to this article can be found online at https://doi.org/10.1016/j.est.2024.112628.

References

[1] B. Yang, J. Wang, P. Cao, T. Zhu, H. Shu, J. Chen, J. Zhang, J. Zhu, Classification, summarization and pers- pectives on state-of-charge estimation of lithium-ion batteries used in electric vehicles: a critical compre- hensive survey, J. Energy Storage 39 (2021) 102572, https://doi.org/10.1016/j.est.2021.102572.

[2] A.A. Franco, A. Rucci, D. Brandell, C. Frayret, M. Gaberscek, P. Jankowski, P. Johansson, Boosting rechar- geable batteries R&D by multiscale modeling: myth or reality? Chem. Rev. 119 (2019) 4569–4627, https://doi.org/10.1021/acs.chemrev.8b00239.

[3] B. Ghalami Choobar, H. Modarress, R. Halladj, S. Amjad-Iranagh, Electrodeposition of lithium metal on lithium anode surface, a simulation study by: kinetic Monte Carlo-embedded atom method, Comput. Mater. Sci. 192 (2021) 110343, https://doi.org/10.1016/j.commatsci.2021.110343.

[4] M. Safari, M. Morcrette, A. Teyssot, C. Delacourt, Multimodal physics-based aging model for life predic- tion of Li-ion batteries, J. Electrochem. Soc. 156 (2009) A145.

[5] X. Hu, S. Li, H. Peng, A comparative study of equivalent circuit models for Li-ion batteries, J. Power Sources 198 (2012) 359–367, https://doi.org/10.1016/j.jpowsour.2011.10.013.

[6] A. Fereydooni, E. Vafa, M.R. Pishvaie, B. Ghalami Choobar, Robust adaptive sliding mode observer for core temperature and state of charge monitoring of Li-ion battery: a simulation study, J. Energy Storage 70 (2023) 107960, https://doi.org/10.1016/j.est.2023.107960.

[7] M. Adaikkappan, N. Sathiyamoorthy, Modeling, state of charge estimation, and charging of lithium-ion battery in electric vehicle: a review, Int. J. Energy Res. 46 (2022) 2141–2165, https://doi.org/10.1002/er.7339.

[8] U.S. Kim, J. Yi, C.B. Shin, T. Han, S. Park, Modelling the thermal behaviour of a lithium-ion battery during charge, J. Power Sources 196 (2011) 5115–5121, https://doi.org/10.1016/j.jpowsour.2011.01.103.

[9] S. Yalçın, S. Panchal, M.S. Herdem, A CNN-ABC model for estimation and optimization of heat generation rate and voltage distributions of lithium-ion batteries for electric vehicles, Int. J. Heat Mass Transf. 199 (2022) 123486, https://doi.org/10.1016/j.ijheatmasstransfer.2022.123486.

[10] H. Pang, L. Wu, J. Liu, X. Liu, K. Liu, Physics-informed neural network approach for heat generation rate estimation of lithium-ion battery under various driving conditions, J. Energy Chem. 78 (2023) 1–12, https://doi.org/10.1016/j.jechem.2022.11.036.

[11] X. Zhang, Y. Wang, Z. Chen, SoC-modified core temperature estimation of lithium-ion battery based on control-oriented electro-thermal model, IEEE Trans. Power Electron. 38 (2023) 11642–11651, https://doi.org/10.1109/TPEL.2023.3288539.

[12] P. Qin, J. Sun, X. Yang, Q. Wang, Battery thermal management system based on the forced-air convection: a review, eTransportation 7 (2021) 100097, https://doi.org/10.1016/j.etran.2020.100097.

[13] X. Hu, L. Xu, X. Lin, M. Pecht, Battery lifetime prognostics, Joule 4 (2020) 310–346, https://doi.org/10.1016/j.joule.2019.11.018.

[14] K.-T. Lee, M.-J. Dai, C.-C. Chuang, Temperature-compensated model for lithium-ion polymer batteries with extended Kalman filter state-of-charge estimation for an implantable charger, IEEE Trans. Ind. Electron. 65 (2018) 589–596, https://doi.org/10.1109/TIE.2017.2721880.

[15] S. Zhang, C. Zhang, S. Jiang, X. Zhang, A comparative study of different adaptive extended/unscented Kalman filters for lithium-ion battery state-of-charge estimation, Energy 246 (2022) 123423, https://doi.org/10.1016/j.energy.2022.123423.

[16] L. Wang, J. Ma, X. Zhao, X. Li, K. Zhang, Z. Jiao, Adaptive robust unscented Kalman filter-based state-of-charge estimation for lithium-ion batteries with multi-parameter updating, Electrochim. Acta 426 (2022) 140760, https://doi.org/10.1016/j.electacta.2022.140760.

[17] L. Chen, X. Wu, A.M. Lopes, L. Yin, P. Li, Adaptive state-of-charge estimation of lithium-ion batteries based on square-root unscented Kalman filter, Energy 252 (2022) 123972, https://doi.org/10.1016/j.energy.2022.123972.

[18] Z. Ning, Z. Deng, J. Li, H. Liu, W. Guo, Co-estimation of state of charge and state of health for 48 V battery system based on cubature Kalman filter and H-infinity, J. Energy Storage 56 (2022) 106052, https://doi.org/10.1016/j.est.2022.106052.

[19] State of Charge estimation for Lithium-ion Battery Based on Hybrid Compensation Modeling and Adaptive H-infinity Filter | IEEE Journals & Magazine | IEEE Xplore, (n.d.). https://ieeexplore.ieee.org/abstract/document/9787508 (accessed September 22, 2023).

[20] L. He, X. Hu, G. Yin, X. Shao, J. Liu, Q. Shi, A voltage dynamics model of lithium-ion battery for state-of-charge estimation by proportional-integral observer, Appl. Energy 351 (2023) 121793, https://doi.org/10.1016/j.apenergy.2023.121793.

[21] X. Chen, W. Shen, Z. Cao, A. Kapoor, A novel approach for state of charge estimation based on adaptive switching gain sliding mode observer in electric vehicles, J. Power Sources 246 (2014) 667–678, https://doi.org/10.1016/j.jpowsour.2013.08.039.

[22] A comprehensive review on the state of charge estimation for lithium-ion battery based on neural network - Cui - 2022 - International Journal of Energy Research - Wiley Online Library, (n.d.). https://onlinelibrary.wiley.com/doi/abs/10.1002/er.7545 (accessed September 22, 2023).

[23] H. Hamed, M. Yusuf, M. Suliga, B. Ghalami Choobar, R. Kostos, M. Safari, An incremental capacity analysis-based state-of-health estimation model for lithium-ion batteries in high-power applications, Batter. Supercaps 6 (2023) e202300140, https://doi.org/10.1002/batt.202300140.

[24] L. Liao, H. Chen, Research on two-stage equalization strategy based on fuzzy logic control for lithium-ion battery packs, J. Energy Storage 50 (2022) 104321, https://doi.org/10.1016/j.est.2022.104321.

[25] C. Xu, E. Zhang, K. Jiang, K. Wang, Dual fuzzy-based adaptive extended Kalman filter for state of charge estimation of liquid metal battery, Appl. Energy 327 (2022) 120091, https://doi.org/10.1016/j.apenergy.2022.120091.

[26] N. Valencia, A. Fotouhi, N. Shateri, D. Auger, Development of a hybrid adaptive neuro-fuzzy inference system with coulomb-counting state-of-charge estimator for lithium–sulphur battery, Int. J. Fuzzy Syst. 25 (2023) 407–422, https://doi.org/10.1007/s40815-022-01403-y.

[27] X. Tang, C. Zou, T. Wik, K. Yao, Y. Xia, Y. Wang, D. Yang, F. Gao, Run-to-run control for active balancing of lithium iron phosphate battery packs, IEEE Trans. Power Electron. 35 (2020) 1499–1512, https://doi.org/10.1109/TPEL.2019.2919709.

[28] M.A. Hannan, M.S.H. Lipu, A. Hussain, A. Mohamed, A review of lithium-ion battery state of charge estimation and management system in electric vehicle applications: challenges and recommendations, Renew. Sust. Energ. Rev. 78 (2017) 834–854, https://doi.org/10.1016/j.rser.2017.05.001.

[29] J.-J.E. Slotine, W. Li, Applied Nonlinear Control, Prentice Hall, Englewood Cliffs, NJ, 1991.

[30] C. Xu, E. Zhang, S. Yan, K. Jiang, K. Wang, Z. Wang, S. Cheng, State of charge estimation for liquid metal battery based on an improved sliding mode observer, J. Energy Storage 45 (2022) 103701, https://doi.org/10.1016/j.est.2021.103701.

[31] B. Ning, B. Cao, B. Wang, Z. Zou, Adaptive sliding mode observers for lithium-ion battery state estimation based on parameters identified online, Energy 153 (2018) 732–742, https://doi.org/10.1016/j.energy.2018.04.026.

[32] I.S. Kim, Nonlinear state of charge estimator for hybrid electric vehicle battery, IEEE Trans. Power Electron. 23 (4) (2008) 2027–2034, https://doi.org/10.1109/tpel.2008.924629.

[33] J. Du, Z. Liu, Y. Wang, C. Wen, An adaptive sliding mode observer for lithium-ion battery state of charge and state of health estimation in electric vehicles, Control. Eng. Pract. 54 (2016) 81–90, https://doi.org/10.1016/j.conengprac.2016.05.014.

[34] Y. Huangfu, J. Xu, D. Zhao, Y. Liu, F. Gao, A novel battery state of charge estimation method based on a super-twisting sliding mode observer, Energies 11 (2018) 1211, https://doi.org/10.3390/en11051211.

[35] M. Gholizadeh, A. Yazdizadeh, State of charge estimation of a lithium-ion battery using robust non-linear observer approach, IET Electr. Syst. Transp. 9 (2019) 1–7, https://doi.org/10.1049/iet-est.2018.0002.

[36] Y. Xie, W. Li, X. Hu, M.-K. Tran, S. Panchal, M. Fowler, Y. Zhang, K. Liu, Coestimation of SOC and three-dimensional SOT for lithium-ion batteries based on distributed spatial–temporal online correction, IEEE Trans. Ind. Electron. 70 (2023) 5937–5948, https://doi.org/10.1109/TIE.2022.3199905.

[37] Y. Ma, Y. Cui, H. Mou, J. Gao, H. Chen, Core temperature estimation of lithium-ion battery for EVs using Kalman filter, Appl. Therm. Eng. 168 (2020) 114816, https://doi.org/10.1016/j.applthermaleng.2019.114816.

[38] D. Mitra, S. Mukhopadhyay, UKF Based Estimation of SOC and Core Temperature of a Lithium Ion Cell Using an Electrical Cell Model, in: 2018 15th IEEE India Counc. Int. Conf. INDICON, IEEE, Coimbatore, India, 2018, pp. 1–6, https://doi.org/10.1109/INDICON45594.2018.8987074.

[39] Y. Wei, L. Ling, State-of-charge estimation for lithium-ion batteries based on temperature-based fractional-order model and dual fractional-order Kalman filter, IEEE Access 10 (2022) 37131–37148, https://doi.org/10.1109/ACCESS.2022.3163413.

[40] N.T. Tran, T. Farrell, M. Vilathgamuwa, S.S. Choi, Y. Li, A computationally efficient coupled electrochemical-thermal model for large format cylindrical lithium ion batteries, J. Electrochem. Soc. 166 (2019) A3059–A3071, https://doi.org/10.1149/2.1241913jes.

[41] L. Wei, Z. Lu, F. Cao, L. Zhang, X. Yang, X. Yu, L. Jin, A comprehensive study on thermal conductivity of the lithium-ion battery, Int. J. Energy Res. 44 (2020) 9466–9478, https://doi.org/10.1002/er.5016.

[42] H. Hamed, B.G. Choobar, S. Hamtaei, J. D'Haen, B. Vermang, M. Safari, Experimental investigation of a 64 Ah lithium-ion pouch cell, J. Electrochem. Soc. 171 (2024) 020510, https://doi.org/10.1149/1945-7111/ad24c2.

[43] L. Sun, G. Li, F. You, Combined internal resistance and state-of-charge estimation of lithium-ion battery based on extended state observer, Renew. Sust. Energ. Rev. 131 (2020) 109994, https://doi.org/10.1016/j.rser.2020.109994.

[44] Y. Feng, C. Xue, Q.-L. Han, F. Han, J. Du, Robust estimation for state-of-charge and state-of-health of lithium-ion batteries using integral-type terminal sliding-mode observers, IEEE Trans. Ind. Electron. 67 (2020) 4013–4023, https://doi.org/10.1109/TIE.2019.2916389.

[45] L. Chen, M. Hu, K. Cao, S. Li, Z. Su, G. Jin, C. Fu, Core temperature estimation based on electro-thermal model of lithium-ion batteries, Int. J. Energy Res. 44 (2020) 5320–5333, https://doi.org/10.1002/er.5281.

[46] Y. Zhou, H. Deng, H.-X. Li, Optimal-sensing-based recursive estimation for temperature distribution of pouch-type batteries, IEEE Trans. Transp. Electrif. 9 (2023) 912–919, https://doi.org/10.1109/TTE.2022.3171857.
[47] Y. Xing, W. He, M. Pecht, K.L. Tsui, State of charge estimation of lithium-ion batteries using the open-circuit voltage at various ambient temperatures, Appl. Energy 113 (2014) 106–115, https://doi.org/10.1016/j.apenergy.2013.07.008.
[48] G. Zhang, L. Cao, S. Ge, C.-Y. Wang, C.E. Shaffer, C.D. Rahn, In situ measurement of radial temperature distributions in cylindrical Li-ion cells, J. Electrochem. Soc. 161 (2014) A1499, https://doi.org/10.1149/2.0051410jes.
[49] Y.A. Çengel, A.J. Ghajar, Heat and Mass Transfer: Fundamentals & Applications, Sixth edition, McGraw-Hill Education, New York, NY, 2020.
[50] J. Landesfeind, J. Hattendorff, A. Ehrl, W.A. Wall, H.A. Gasteiger, Tortuosity determination of battery electrodes and separators by impedance spectroscopy, J. Electrochem. Soc. 163 (2016) A1373–A1387, https://doi.org/10.1149/2.1141607jes.
[51] A. Loges, S. Herberger, D. Werner, T. Wetzel, Thermal characterization of Li-ion cell electrodes by photothermal deflection spectroscopy, J. Power Sources 325 (2016) 104–115, https://doi.org/10.1016/j.jpowsour.2016.05.082.